Original Paper

Determination of shale macroscale modulus based on microscale measurement: A case study concerning multiscale mechanical characteristics

Yong Li [a, *], Jian-Qi Chen [a], Jiang-Hao Yang [a], Ji-Shan Liu [b], Wang-Shu Tong [c]

[a] State Key Laboratory of Coal Resources and Safe Mining and College of Geosciences and Surveying Engineering, China University of Mining and Technology (Beijing), Beijing, 100083, China
[b] School of Mechanical and Chemical Engineering, The University of Western Australia, 35 Stirling Highway, Perth, WA, 6009, Australia
[c] School of Material Science and Engineering, China University of Geosciences(Beijing), Beijing, 100083, China

ARTICLE INFO

ABSTRACT

Shale mechanical properties are important for shale gas production, but the magnitudes are difficult to estimate, standard size cores are hard to sample, and secondary interstice generation is inevitable. This paper proposes a method for determining shale macroscale modulus, which is determined at a hierarchy of scales from the nano-to macro-scales. Microscale measurements are upscaled to estimate the corresponding magnitudes at the macroscale. A case study is conducted with Silurian shale samples, using the hierarchy scales, gridding nanoindentation, atomic force microscopy (AFM), mineral liberation analysis (MLA), X-ray diffraction (XRD), and uniaxial compression tests. The mineral compositions are analyzed using MLA and XRD, and the shale composition is described in terms of clay minerals, organic matter, and siliceous and carbonate contents. The variation in the Young's modulus is analyzed based on the recorded indentation depth curves and modulus distributions. The nanoindentation and AFM results are upscaled to the centimeter scale through the Mori−Tanaka method. The upscaled results exhibit satisfactory fitting with the conventional uniaxial compression results, although the fitting of the upscaled AFM results is better than nanoindentation. The proposed approach can be applied to promptly and comprehensively predict the shale mechanical parameters during shale gas exploration.

1. Introduction

Shale gas and oil are key commodities in the current energy market as with new technologies emergence (Gilbert et al., 2014; Wu et al., 2020; Li et al., 2022). During shale gas/oil exploration, the rock mechanics, such as the elastic modulus and its anisotropy, significantly influence the interpretation of the seismic data and the establishment of geological models (Thomas et al., 2016). Moreover, in well drilling, the shale mechanics are considerably influenced by aspects such as the well instability and low drilling speed (Cai et al., 2018). Thus, it is necessary to accurately determine the rock modulus, hardness, and strength parameters to clarify the complex wellbore conditions and prevent accidents (Delafargue et al., 2004). In hydraulic fracturing, the hardness and elastic modulus must be determined to evaluate the reservoir property. Moreover, the mechanical characteristics of the rock can provide guidance to realize well completion and segmentation, compressibility evaluation, and proppant selection (Fallahzadeh et al., 2015).

As a porous medium, shale is composed of organic matter and various minerals and includes several laminae, fractures, and joints developed during the deposition and tectonic evolution history (Wang et al., 2015; Dong and Chen. 2017). Different minerals have significantly different mechanical properties, and these differences become more notable when intra-generated pores and microfractures are generated (Raoof et al., 2018). In addition, the pore structure distribution of shale exhibits a strong heterogeneity, as the pores are influenced by the sedimentary, diagenesis, and thermal evolution history (Raoof et al., 2016; Li et al., 2017). The rock mass likely experienced irreversible deformation under the action of external forces during the geological history, resulting in

* Corresponding author.
 E-mail address: liyong@cumtb.edu.cn (Y. Li).

List of symbols

E_r	the reduced modulus, GPa
E	Young's modulus, GPa
E_i	Young's modulus for the diamond indenter or probe, GPa
S	the unloading indentation stiffness, N/m
A_c	the contact area, m^2
h	the contact depth, nm
h_{max}	the maximum displacement, nm
P	measured maximum indentation load
F_{tip}	the force on the tip, mN
F_{adh}	the adhesion force, mN
R	the tip radius, nm
d	the sample deformation, mm
K_J	the bulk of phase J

G_J	shear modulus of phase J, GPa
E_J	Young's modulus of phase J, GPa
K_c	bulk of solid particles in the clay, GPa
G_c	shear modulus of solid particles in the clay, GPa
K_0	bulk modulus of the porous matrix, GPa
G_0	shear modulus of the porous matrix, GPa
K_M	bulk modulus after homogenization, GPa
G_M	shear modulus after homogenization, GPa
E_M	homogenized Young's modulus, GPa

Greek letters

ν	Poisson's ratio
ν_i	Poisson's ratio values for the diamond indenter or probe
ν_J	Poisson's ratio of phase J
φ	porosity, %

macro fractures and deformations (Hakala et al., 2007; Ju et al., 2018). Such macro and microscale structures contribute to the discontinuity, inhomogeneity, and anisotropy of shale, and considerably influence the rock deformation behavior during well drilling and engineering (Han et al., 2018; Hu and Li, 2015). Therefore, the geological evolution of shale, along with the orientation of the mineral particles and the superposition of the fractures induced during coring operations, contributes to the strong heterogeneity of shale (Huang et al., 2012).

Although logging curves, such as sonic and density logging data, have been commonly used to simulate the mechanical parameters, laboratory test data are more widely applied to realize engineering design and compare rocks with different lithologies (Ilgen et al., 2017; Josh et al., 2012; Kivi et al., 2018). Conventional rock mechanical tests, including uniaxial and triaxial compression tests, are commonly performed to obtain the relevant parameters (Gathier et al., 2008; Gholami et al. 2016, 2018). However, the use of routine core testing during the time-sensitive shale gas production process is undesirable owing to the time-consuming sampling process and restrictive requirements in terms of the specimen size and integrity (Lferobia et al., 2019; Li et al. 2018, 2019). In addition, owing to the heterogeneity of shale, the routine tests based on continuum cores cannot fully clarify the microscopic variations induced by the micro and macro pores and laminae.

To overcome these limitations, microscopic methods are being increasingly used to examine the microscopic mechanical properties of specific minerals and kerogens. Such approaches include X-ray diffraction (XRD) and nanoindentation based approaches to clarify the factors influencing the indentation curves (Li and Bhushan, 2002; Liu et al., 2018), backscattering electron (BSE) diffraction and nanoindentation to study the kerogen mechanical properties (Li et al., 2017; Liu et al., 2016), and atomic force microscopy (AFM) and scanning electron microscopy (SEM) to investigate the elastic parameters of a certain domain (Zhao et al., 2019; Li et al., 2020). With the development of micro and nano measurement technologies, the equivalent homogenization theory to evaluate the macroscale mechanical parameters has also been established (Lucas et al., 1998; Liu et al., 2019). A basis for such homogenization is to establish the relationship between the rock compositions and elastic constants, and subsequently, to upscale the micro characteristics to reveal the macro behaviors (Mori et al., 1973; Niandou et al., 1997).

In this work, the shale macroscale modulus was determined based on nanoscale and microscale measurements. AFM and nanoindentation techniques were combined to examine the

microscopic mechanical properties of shale samples. Subsequently, the effectiveness of these techniques was evaluated by upscaling the nano and micrometer scale results to millimeter and centimeter scales. The presented findings can enable the prompt determination of the mechanical properties of shale during well drilling, as the rock debris can be used to clarify the macro elastic constants. And the method can also be applied for engineering issues associated with unconventional reservoirs, e.g., shale gas, shale oil and coalbed methane, as well as engineering designs in shale or mudstone deposited strata.

2. Material and methods

Basic procedure: Both macro and micro scale measurements were performed to compare and validate the results. Owing to the different sample size and processing requirements for different techniques, the routine uniaxial compression test was first performed. Subsequently, 5mm × 10mm × 20 mm section was prepared from the same sample and subjected to argon ion polishing. The slice size and morphology can be adjusted according to the characteristics of different debris and particles. After that, the slices were subjected to nanoindentation. Next, the AFM test was conducted, for nanoscale measurements. The deformation caused by the nanoindentation was recorded during the AFM test. Finally, the slices were tested using a mineral liberation analyzer (MLA), because in this approach, the sample is required to be coated with carbon or gold to achieve higher resolutions. XRD testing was performed using the debris acquired during the sample preparation to validate the MLA results (Fig. 1).

During the upscaling process, the nanoindentation and AFM results were first analyzed to determine the microscale modulus of shale. Then, the MLA results were integrated, with the mineral compositions classified on the basis of the modulus differences. Subsequently, upscaling was performed using the Mori–Tanaka method after a literature survey and comparison of the several different approaches available for upscaling (Sangwal, 2000; Oliver et al., 2004; Pakzad et al., 2012).

Sample preparation: The shale mass was sampled from the Lower Silurian Longmaxi Formation in the Changning area, Sichuan Basin. In general, the Silurian Longmaxi Formation shale is rich in organic matter with a high content of residual organic carbon around 2%–3%. The vitrinite reflectance (R_o) of the samples ranges from 2.22% to 2.89%, averaging of 2.55%, indicating a relatively high degree of thermal maturity.

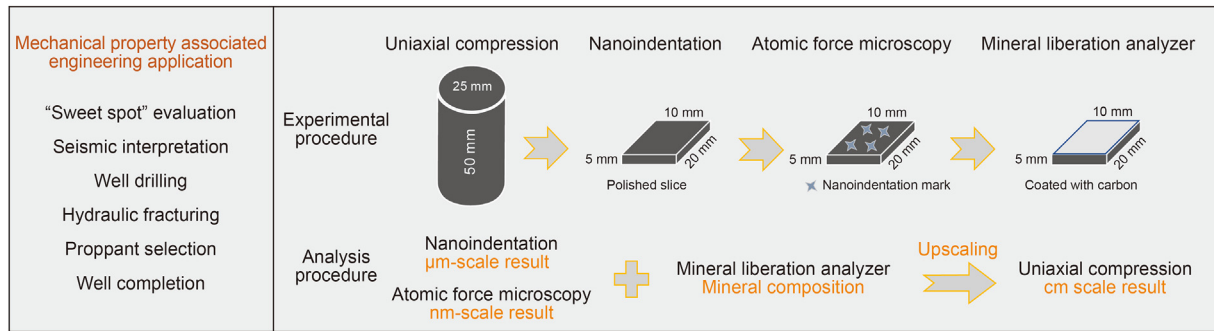To prepare the samples, the shale was drilled into standard

Fig. 1. Experimental procedure to determine the macroscale modulus based on microscale measurements.

cylinders of 25 mm × 50 mm by line cutting machine. Samples a_v and b_v were perpendicular to the bedding, and samples a_p and b_p were parallel to the bedding. The instrument operates in a displacement-controlled mode with a loading rate of 0.05 mm/min. When the strain of rock reaches a certain degree, the test is stopped and the compression curve is recorded. From the same shale mass, samples of 20 mm × 10 mm × 5 mm were cut for the micro-mechanical testing. The slices were prepared along the core direction. Among the four slices, 1_p and 2_p were parallel to the bedding, and 1_v and 2_v were perpendicular to beddings and all of them were polished by argon ion.

XRD: The mineral composition of the whole rock was determined using an XRD device (D/max-PC2500X), operated using a Cu X-ray tube at 40 kV and 30 mA. Counts were collected from 3° to 90° with a step size of 0.02° and a speed of 3°/min. A fresh sample (approximately 50 g) was crushed into powders smaller than 80 mesh, and 10 g of the sample was grinded in an agate mortar until the powder corresponded to 300 mesh. The prepared sample was placed on the test instrument, and the appropriate parameters were adjusted to obtain the mineral composition.

MLA: The instrument used in MLA experiment is FEI MLA250. The MLA is a type of mineral automatic analysis and test equipment, and the energy dispersive X-ray fluorescence spectrometer can be used to realize the automatic scanning and energy spectrum analysis. An MLA includes a scanning electron microscope, X-ray spectrometer, and software package. The software allows for measurement, image processing, mineral editing, and data output. Firstly, the SEM images of the sample were obtained at 25 kV acceleration voltage and 10 nA beam current. Subsequently, using the X-rays in pixels, different mineral phases were distinguished by considering the difference in the gray values, and the minerals could be identified rapidly and synchronously.

Nanoindentation: Nano Indenter G200 from Keysight Technologies was used for nanoindentation, and the test site was Tsinghua University. In this process, the tip of the indenter slowly contacts the sample surface, and the penetration depth and applied load are recorded. The process of nanoindentation can be divided into the loading, constant loading, and unloading stages. In the loading stage, when a small load is applied by the indenter on the surface of the material, elastic deformation occurs in the indentation region. As the load increases, elastoplastic and plastic deformation occur in the region with the greatest elastic deformation. When the load is sufficiently large, the compression region enters the complete plastic stage. In the unloading stage, when the test indenter is withdrawn, elastic recovery occurs in the previously loaded area. The hardness can be calculated according to the unloading curve, and the elastic modulus of the test material can be evaluated.

Using the reduced modulus E_r and Poisson's ratio v, Young's

modulus of the shale E can be calculated by

$$\frac{1}{E_r} = \frac{1-v^2}{E} + \frac{1-v_i^2}{E_i} \tag{1}$$

where E_i and v_i denote the Young's modulus and Poisson's ratio values for the diamond indenter or probe, respectively (Bennett et al., 2015). E_r is the reduced modulus which can be calculated from Eq.(2):

$$E_r = \frac{\sqrt{\pi} S}{2\sqrt{A_c}} \tag{2}$$

$$S = \left(\frac{dP}{dh}\right)_{h=h_{max}} \tag{3}$$

Here A_c is the contact area and S is the unloading indentation stiffness which is quantified as the slope of the upper portion of the unloading curve, h is the contact depth and P is the measured maximum indentation load.

The equipment used in this study involved a Berkovich pyramidal indenter to measure the rock mechanical properties. The indentation apparatus had a displacement resolution of 0.01 nm, and a load resolution of 100 nN during standard loading.

To reveal the heterogeneous characteristics of the considered samples and obtain the Young's modulus values for different components, several indents were required to be created to accurately represent the mechanical properties of the sample. A 5 × 5 indentation grid was used to test the shale. In the process of sample preparation, due to the possible damage to the sample surface, the maximum pressure used this time is 400 mN, in order to make the measured data more representative. The distance between the indentation points was 100 μm, which was larger than the characteristic size of the mineral. The nano indenter approached the surface of the sample at a load drop rate of 30 nm/s. When the test system indicated that the load suddenly increased, the indenter was considered to contact the surface of the sample. At this instant, the system began loading and automatically recorded the load and depth according to the set mode. When the peak force (400 mN) was attained, the loading was maintained for 15 s to eliminate the influence of rock creep on the unloading performance (Shen et al., 2013; Shen and Shao, 2016).

AFM: The key to measure Young's modulus of shale is to select suitable probe. For a given cantilever spring constant, there is a limited range of moduli that can be measured. Pittenger et al. (2014) provide the working ranges of commercially available cantilevers and calibration standards. The basic principle of selecting probe is: the cantilever must be hard enough to ensure that the sample has enough deformation; the cantilever must be soft

enough to ensure sufficient detection sensitivity. Because shale often contains hard minerals such as quartz and pyrite, diamond probe is selected (DNISP; Bruker; spring constant 350 N/m; tip radius 40 nm). The advantage of DNISP probe is that it can theoretically measure the mechanical parameters of all components in shale.

Several calibrations must be performed in order to receive quantitatively reliable outcomes. First, we need to measure the deflection sensitivity. The purpose of calculating the parameter is to convert the spot offset into the actual bending of the cantilever, and then study the mechanical properties. There are two steps in the measurement of reflection sensitivity: 1) obtaining the force curve on sapphire surface; 2) The contact area between the probe and the sample on the force curve is selected to calculate the reflection sensitivity. In order to make the calculation results accurate, it is necessary to measure the sapphire surface for many times, so that the error of the obtained value is within 5%. Second, the cantilever spring constant was calibrated by the instrument producer. The calibration spring constant provided by this calibration was equal to 350N/m. Third, Adjust the tip radius until the average modulus of DMT module data is consistent with that of the standard sample, and record the tip radius for the measurement of the actual sample. All the above steps are strictly referred to the operation manual. The AFM images and force−distance curves were recorded at room temperature (20 °C) using a Dimension Icon AFM from the Bruker Company, Germany. The indentation area was determined using the optical microscope in the device, and the indentation points were scanned sequentially using the PeakForce quantitative nanomechanical mapping (PF-QNM) mode. The force−distance curves of each scanning point were recorded in real time. The PF-QNM mode allows for the mapping of the mechanical properties simultaneously with the topography at the same spatial resolution (Shukla et al., 2013; Li et al., 2018). The digital resolution was 256 × 256 pixels, and the scanning rate was 0.977 Hz. The maximum force ranged from 50 to 250 nN.

The Derjaguin−Muller−Toporov (DMT) model was used to calculate reduced modulus E_r:

$$F_{tip} = \frac{4}{3} E_r \sqrt{Rd^3} + F_{adh} \tag{4}$$

where F_{tip} is the force on the tip, F_{adh} is the adhesion force, R is the tip radius, d is the sample deformation. The young's modulus of the sample can be obtained by introducing the calculated reduced modulus into Eq (1).

3. Results

3.1. Rock compositions

The mineral composition was quantitatively determined by analyzing the XRD scanning signal peaks. The results indicated that the primary mineral components are clay minerals (40.36%), quartz (35.41%), calcite (12.51%) and dolomite (9.55%). The proportion of brittle minerals such as quartz, calcite, and dolomite are relatively high, indicating that the shale is of certain brittleness.

The mineral distribution around the indentation area of the four tested samples was determined using the MLA (Fig. 2). In particular, because different image resolutions can be acquired using MLA, detailed mineral compositions can be conveniently obtained. The main minerals included quartz, calcite, dolomite, pyrite, and clay minerals. In addition, organic matter was observed along the particle edges. The mineral particles were generally well compacted, with the macro pores being almost undeveloped. The statistical results indicated that the main mineral composition of the sample included quartz (31.3%) and clay minerals (40.6%), followed by carbonate minerals, accounting for 19.8% of the scanning area. The mineral composition tested by MLA is generally coincident with the XRD results. Table 1 lists the minerals with contents greater than 1%. In general, mineral compositions have a significant impact on the mechanical properties of shale, and each mineral has a certain modulus range (Shea and Kronenberg, 1993; Prasad et al., 2005). However, the MLA results indicate that it is difficult to classify each mineral during the upscaling procedure. Therefore, minerals can be divided into three groups (clay minerals, siliceous minerals and carbonates minerals) according to their contents and mechanical responses.

Moreover, the MLA can only get the area fraction of mineral distribution, but not reflect the volume fraction accurately. The XRD results provided a good reference for the mineral content, and it was noted that the contents of the main elements such as quartz, calcite, and dolomite were not considerably different. Therefore, it was considered that the four tested slices, two perpendicular and two parallel to the bedding, could generally represent the mineral composition of the entire rock.

3.2. Microscale results obtained via nanoindentation

3.2.1. Nanoindentation curves

The elastic−plastic deformation curves corresponding to the loading process were as shown in Fig. 3. When the indenter encounters the surface of the sample, elastic deformation occurs firstly and followed by plastic deformation as with pressure increment. This process can be considered as a combination of elastic and plastic transformations (Liu and Ostadhassan, 2017). The indentation depths are generally deeper than 2000 nm, with the average indentation depths for samples 1_v, 2_v, 1_p and 2_p being 2969.8, 3153.9, 3046.1, and 3044.8 nm, respectively. The maximum indentation depth corresponded to sample 1_p, ranges from 2550.2 nm to 3953.2 nm (Table 2). After unloading, the curves did not return to the original position, indicating that the sample underwent plastic deformation with increase in the residual depth. The results for the samples parallel and perpendicular to the bedding did not indicate any notable differences.

The load−displacement curves provide valuable mechanical information that can be used to calculate the modulus and hardness of the specimen and identify the occurrence of nonlinear events such as phase transformations, cracking, and delamination (Ulm et al., 2005). Two special indentation curves were obtained, as shown in Fig. 4. And Fig. 4a shows the "pop-in" phenomenon in the loading curve, which occurred owing to the generation of cracks. This phenomenon often occurs in the loading curve of layered materials such as shale. Fig. 4b indicates a normal pattern of the loading curve. However, the unloading curve follows an "elbow" pattern. The pressure beneath the indenter is extremely high and increases with increase in the indentation depth. Phase transformation occurs when the hydrostatic pressure is higher than the critical value (Ulm et al., 2006; Veytskin et al., 2017). The gradual variation of the unloading curve is a result of the material expansion during the slow transformation to the amorphous phase, which contributes to the lifting of the indenter (Domnich et al., 2000).

Fig. 5 shows the surface features of the undamaged sample, in which Fig. a c e g show the morphology, and Fig. b d f h show the corresponding Young's modulus distribution. The topography reflects the height fluctuation of the sample surface, while the Young's modulus images reflect the mechanical properties of each point on the sample surface.
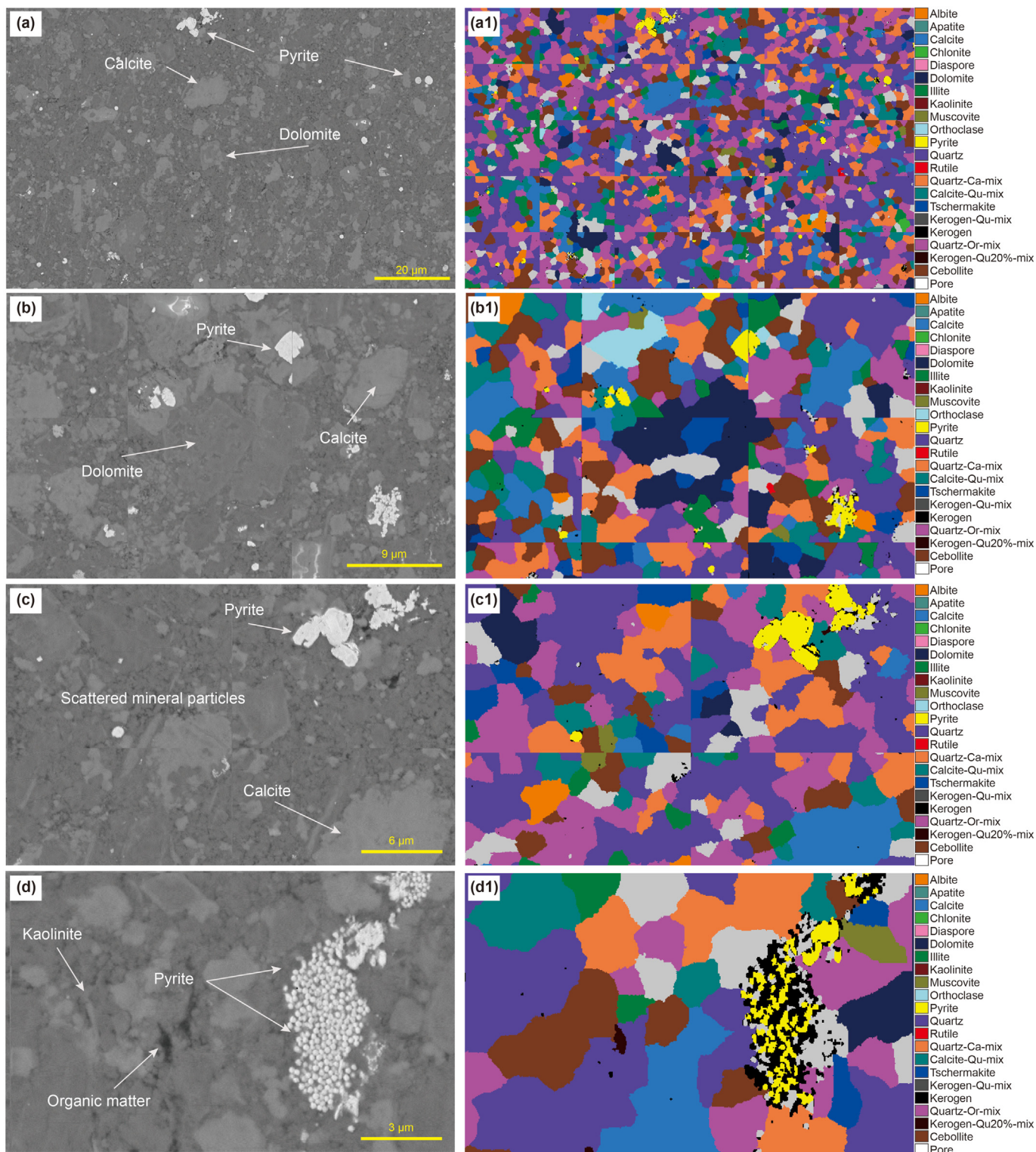
Fig. 2. Mineral distribution obtained using mineral-liberation-analyzer (MLA)-based analysis (Sample 1v). The left is the electron microscope image, and the right is the mineral distribution image of the same area, which is gradually enlarged *a* to *d*.

3.2.2. Distribution of Young's modulus

The Young's modulus values are not considerably different among the four samples. Specifically, the average Young's modulus is approximately 53.55, 47.12, 52.57, and 50.88 GPa for samples 1_v, 2_v, 1_p and 2_p. In combination with the MLA results, it can be concluded that a strong correlation exists between the quartz mineral content and Young's modulus: a higher quartz content corresponds to a larger modulus (Milliken et al., 2012; Milliken and Olson, 2017; Xu et al., 2021). The hardness of the samples was also recorded, and the values were 2.54, 2.22, 2.44 and 2.29 GPa for

Table 1
Composition analysis of the samples considering the area fraction (%) determined using a mineral liberation analyzer (MLA).

Mineral	Sample 1_v, %	Sample 2_v, %	Sample 1_p, %	Sample 2_p, %
Clay	39.3	35.6	43.1	44.7
Quartz	34.7	30.6	32.3	27.7
Dolomite	3.6	19.0	14.2	3.76
Calcite	8.2	2.7	0.8	10.2
Pyrite	1.4	1.6	1.5	0.8
Organic matter	3.9	2.0	2.0	3.1

samples 1_v, 2_v, 1_p and 2_p.

With the increase in the indentation depth, the Young's modulus values decrease (Fig. 6a). In contrast, the hardness values vary in the form of a power low function with a variance of 0.986 (Fig. 6b). In the low loading area, the indenter presses into only the shallow layer of the material surface. At this time, the hardness and Young's modulus depend mainly on the strain distribution of the material surface. The surface damage caused by the indentation process appears in the form of residual stress or plastic deformation. When the indentation depth increases, the work of the indenter is converted into plastic deformation energy, and the residual stress in the material decreases. Thus, the hardness and elastic modulus decrease, and the extra work applied to the indentation size change (Wawersik and Fairhurst, 1970).

3.3. Nanometer scale results obtained using AFM

The topography obtained via the AFM analysis illustrates the fluctuation of the shale surfaces (Fig. 4c). The Peak force error images show the details of the sample surface more clearly (Fig. 4f). The average modulus and area fraction of each phase were determined via bearing analysis. Fig. 7 shows the distribution of Young's modulus of the shale surface, obtained using AFM. Different peaks, representing different strength phases, can be observed from the histogram distribution. The average modulus and area fraction of different phases were obtained using the Nanoscope software, and the results are presented in Table 3. The shale samples were drilled at the same location, and the modulus distribution ranges of the four samples are lower than the range corresponding to 120 GPa. However, the average value and area fraction of the different phases are considerably different. A trimodal distribution is observed for samples 1_v and 1_p. Sample 2_v exhibits a uniform distribution between 0 and 80 GPa, and the peak diffraction is not obvious. For sample 2_p, the peak of the Young's modulus between 30 and 70 GPa is quite high, indicating that the region corresponding to this mechanical strength is large. Further, the modulus range >100 GPa is reasonably high for sample 2_p, indicating the presence of high-strength minerals. If the troughs around 30 GPa and 60 GPa are considered as separation boundaries, three groups corresponding to low-, medium-, and high-strength phases can be identified. The
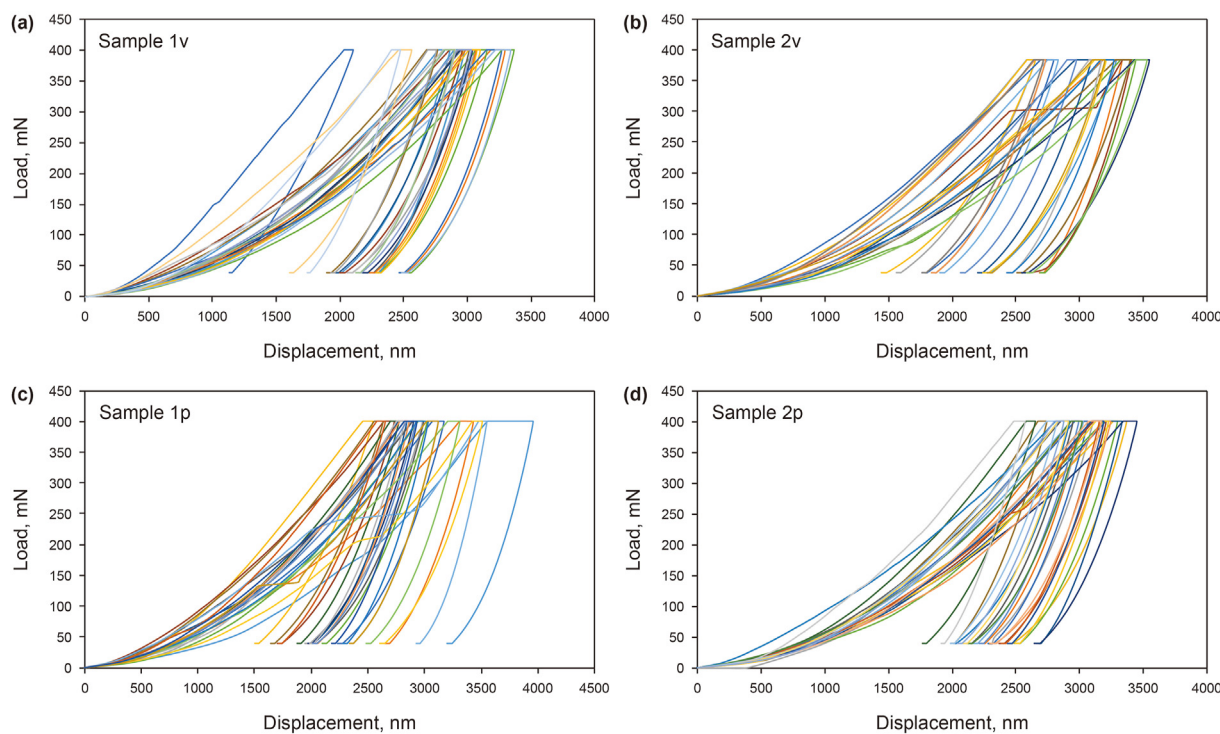
Fig. 3. Indentation curves of the tested samples.

Table 2
Analysis of indentation curve data.

Sample	Minimum depth, nm	Maximum depth, nm	Radius, nm	Average depth, nm
1_v	2039.1	3330.7	1291.6	2969.8
2_v	2708.4	3522.8	814.4	3153.9
1_p	2550.2	3953.2	1403.0	3046.1
2_p	2565.8	3441.4	875.6	3044.8
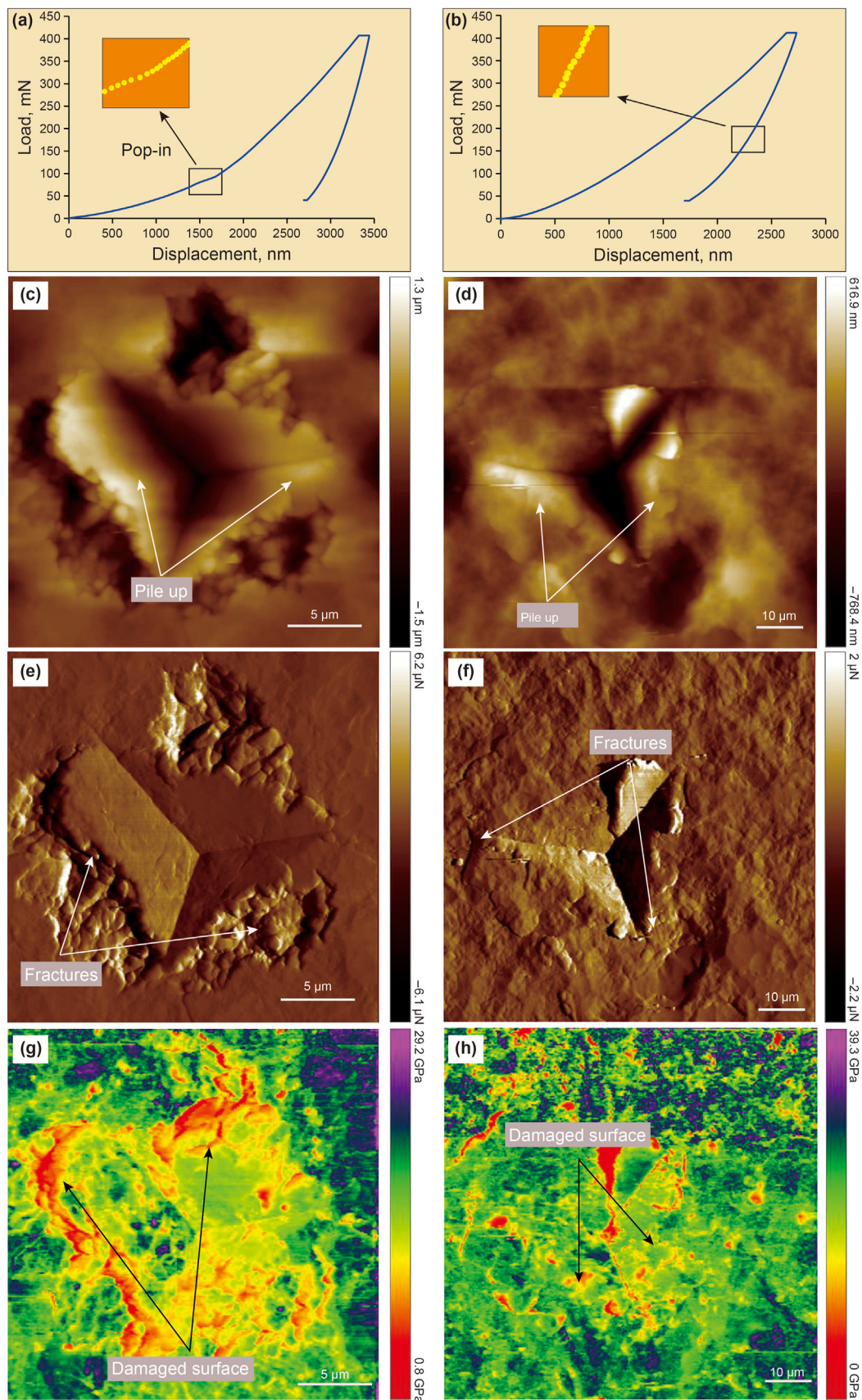
Fig. 4. Two typical indentation curves and corresponding atomic force microscopy (AFM) images: a, b: indentation curves; c, d: topography images; e, f: peak force error images; g, h: Young's modulus images.
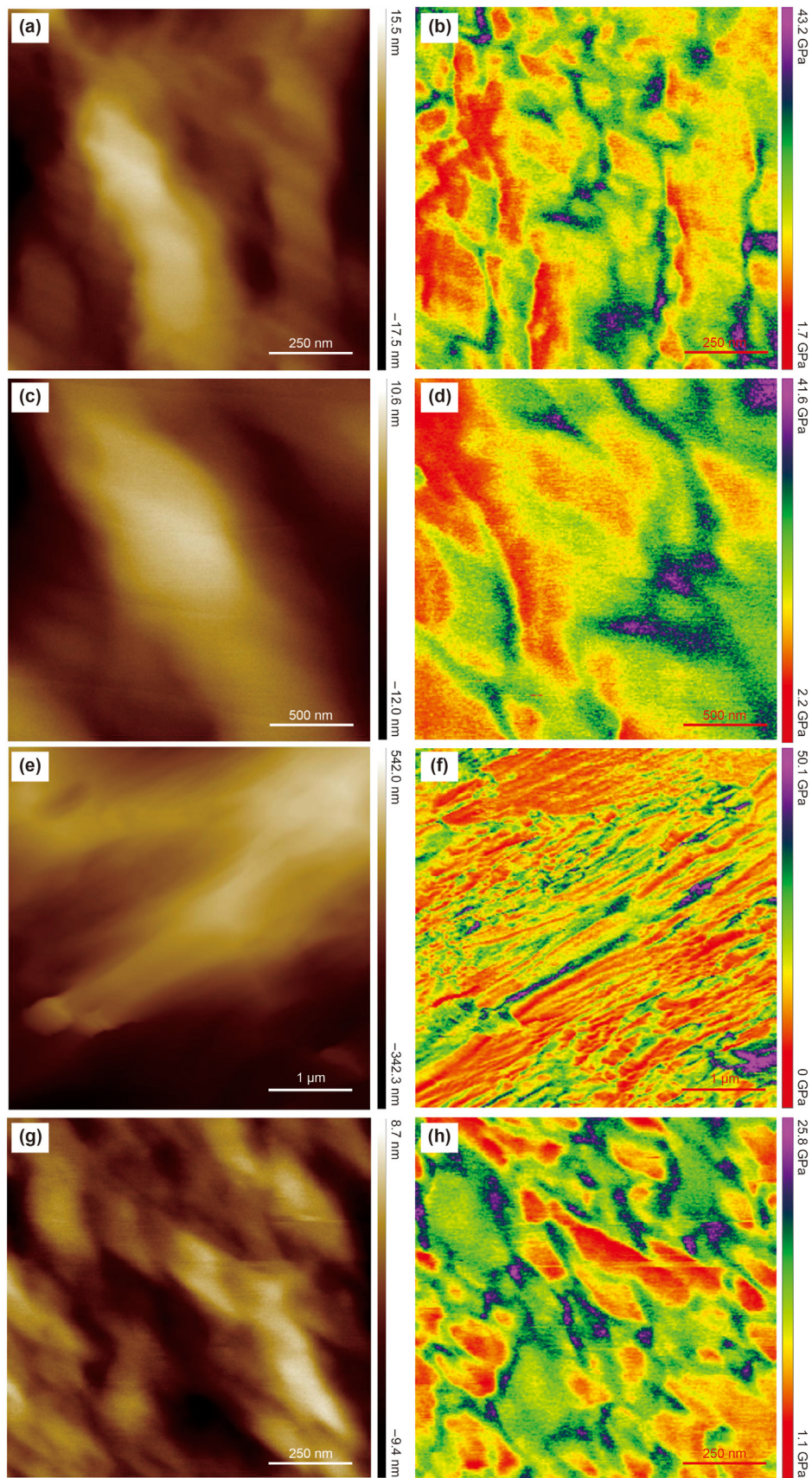
Fig. 5. Select the undamaged surface in the sample for scanning: a, c, e, g are the topography and b, d, f, h are the Young's modulus.
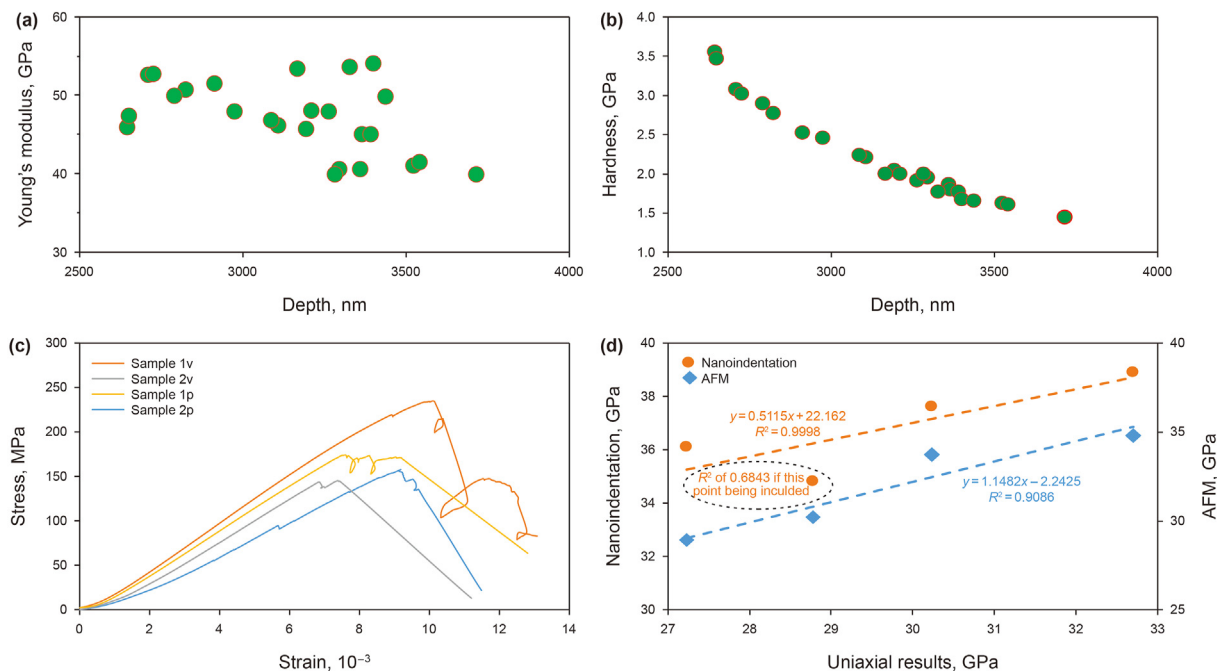
Fig. 6. a: The young's modulus obtained by nanoindentation decrease with the increase of depth; b: The hardness curve is inversely proportional to the depth; c: The stress-strain curve obtained by uniaxial compression; d: The results of Nanoindentation and AFM have a good linear relationship with the strength obtained by uniaxial compression.
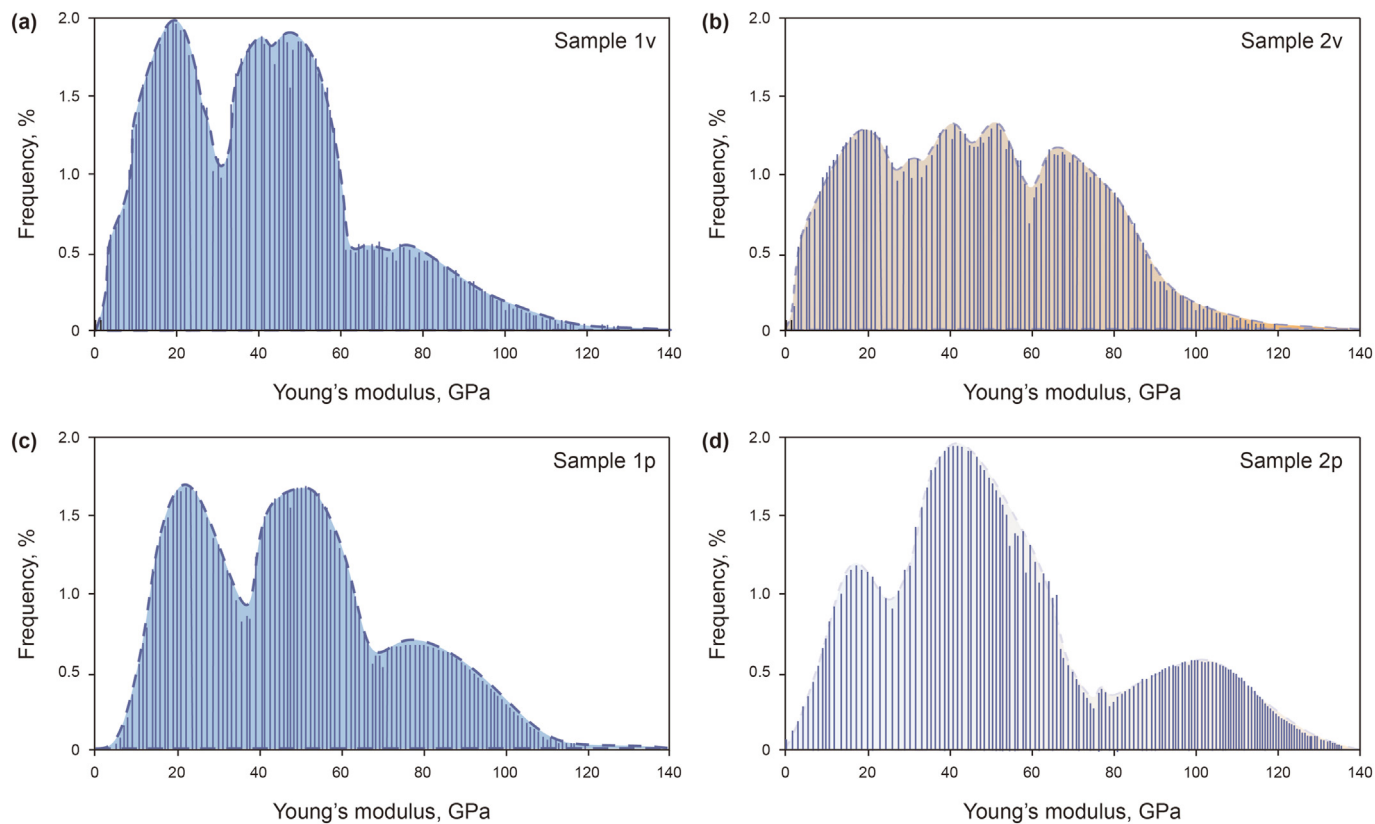
Fig. 7. Distribution of the Young's modulus.

area fractions of the low- and medium-strength phases for samples 1_p and 1_v are similar, although the average modulus of sample 1_v is higher. The area distributions of the three phases for sample 2_v are similar; however, the average value of the high-strength phase is small. The average value of the high-strength phase for sample 2_p is higher.

Table 3
Distribution of modulus area fraction for different peaks.

Sample	Group 1		Group 2		Group 3	
	Average Modulus, GPa	Area Fraction	Average Modulus, GPa	Area Fraction	Average Modulus, GPa	Area Fraction
1_v	28.2	0.48	53.2	0.42	82.6	0.10
2_v	21.3	0.32	47.9	0.33	73.5	0.35
1_p	22.4	0.45	57.7	0.41	77.2	0.24
2_p	18.9	0.38	48.6	0.52	102.6	0.10

Table 4
Uniaxial compression test results.

Sample number	Length, mm	Diameter, mm	Weight, g	Density, g/cm^3	Modulus, GPa	Poisson's ratio
1_v	49.31	25.06	61.65	2.54	32.70	0.21
2_v	49.56	25.06	62.07	2.54	28.78	0.17
1_p	50.16	25.06	61.82	2.50	31.23	0.19
2_p	50.46	25.05	62.25	2.50	27.23	0.17

Table 5
Statistical details for the nanoindentation mechanical parameters for specific minerals.

Mineral Species	Average modulus, GPa	Poisson's ratio	Area Fraction			
			Sample 1_v	Sample 2_v	Sample 1_p	Sample 2_p
Clay minerals	43	0.32	0.39	0.43	0.43	0.45
Siliceous content	96	0.06	0.33	0.31	0.32	0.29
Carbonates	77	0.28	0.19	0.24	0.17	0.18
Organic matter	8	0.20	0.04	0.02	0.02	0.03

3.4. Centimeter-scale results obtained via compression testing

Compression testing was performed on the cores sized 25 cm × 50 cm to obtain the macroscale mechanical properties (Table 4). The modulus of the four samples varies between 27.23 and 32.70 GPa, and the differences are relatively high. The values for samples 1_v and 1_p are similar, approximately 32 GPa; however, the values for samples 2_v and 2_p are 27.23 and 28.78 GPa, respectively. The Poisson's ratio values exhibit differences among the four samples, although the samples perpendicular or parallel to the bedding line do not exhibit a notable difference in terms of these values. This finding likely occurs because the shale samples are tightly deposited, and the lamina is not obvious; consequently, the mechanical parameters are not considerably influenced (see Table 5).

The stress−strain curves determined during the test are shown in Fig. 6c. The upward stage of the curve can be divided into three parts. In the initial stage of loading, the curves exhibit steadily increasing slopes, and the relationship between stress and strain is nonlinear. This relationship is generally more pronounced for looser, more porous rocks and for rocks containing numerous small preexisting fractures (Wilkinson and Fenton, 2015; Xia et al., 2014). The curves in the second zone are nearly linear, indicating elastic behavior of the rock, which provides a basis to measure the Young's modulus values. After this section, the curve slopes decrease slightly, and the rock transitions from the elastic deformation stage to plastic deformation. The minor nonlinear anomaly before the peak was likely caused by the presence of localized micro-cracks and/or compaction effects (Samples 1_v and 2_p). After the peak, the stress decreases rapidly owing to the propagation and penetration of several cracks. Significant differences in the stress−strain curves can be noted in terms of the post-peak behavior. Samples 1v and 2v exhibit the highest and lowest peak strengths, respectively. Samples 1v and 1p exhibit a complex post-peak behavior, involving strong heterogeneity (Yang et al., 2008).

4. Discussion

4.1. Upscaling and homogenization of multi-scale mechanical parameters

4.1.1. Upscaling method

Shale is a mixture of porous clay and non-clay phase media on the micro scale (Zaoui et al., 2002). Therefore, the mechanical parameters of shale at the micro scale can be homogenized. The key for homogenization is to analyze the inherent characteristics of the shale units. The mineral components were determined via the AFM and nanoindentation techniques. The upscaling from microscopic to macroscopic properties was realized using the dilute, self-consistency, and Mori−Tanaka methods (Sangwal, 2000; Oliver et al., 2004; Pakzad et al., 2012). The dilution estimation corresponds to the simplest situation in which the mass involves a small proportion of inclusions. In addition, the concentration of inclusions is sufficiently small such that all the inclusions are well separated (Sangwal, 2000). The self-consistent method treats each phase, solid and pore, of the porous composite as a phase surrounded by the averaged composite (Pakzad et al., 2012). The Mori−Tanaka method considers that the material is composed of multiple inclusion particles, and the strain acting on a single inclusion particle is different from the macroscopic strain at infinity. When considering multiple inclusions, the interaction between the media is considered. Porous materials with a dominating matrix−pore inclusion morphology are well represented by the Mori−Tanaka scheme (Yang et al., 2008). As shale is composed of porous clay mixed with a non-clay phase, having a texture similar to that of the matrix−pore inclusion morphology, the Mori−Tanaka method is suitable for the elastic homogenization of shale (Zeng and Shen, 2002).

The nanoindentation results indicate that the mechanical properties of the different minerals in the sample are considerably different (Table 6). The clay minerals are assumed to constitute the

Table 6
Upscaling result corresponding to nanoindentation and AFM test results.

Sample	K_J, GPa		G_J, GPa		E_M, GPa		Uniaxial Young's modulus, GPa
	Indentation	AFM	Indentation	AFM	Indentation	AFM	
1_v	28.4	33.9	15.3	13.1	38.9	34.8	32.70
2_v	25.3	35.2	13.7	14.0	34.5	30.2	28.78
1_p	26.5	33.1	14.9	13.1	37.6	33.7	30.23
2_p	24.3	29.3	14.4	11.7	36.1	28.9	27.23

matrix, with the siliceous, carbonatite, and organic matter being mixed. The MLA test results were used to determine the Young's modulus and area fractions of each grade. To simplify the calculation process, the minerals detected using the MLA were classified into four groups: clay minerals, siliceous content, carbonate content, and organic matter (Fig. 8). Subsequently, the average Young's modulus and area fraction of the four types of minerals were determined to calculate the Young's modulus at the core scale.

The Mori–Tanaka method approximates the interaction between different phases, assuming that each inclusion is embedded. In this study, clay minerals were used as the reference medium to calculate the equivalent Young's modulus of shale at the core scales. For materials composed of M-phase media, the homogenized bulk and shear modulus can be calculated as

$$K_M = \left(\sum_J f_J \frac{K_J}{4G_0 + 3K_J}\right)\left(\sum_J \frac{f_J}{4G_0 + 3K_J}\right)^{-1} \tag{5}$$

$$G_M = \frac{\sum_J f_J \frac{G_J}{G_0(8G_0+9K_0)+6G_J(2G_0+K_0)}}{\sum_J \frac{f_J}{G_0(8G_0+9K_0)+6G_J(2G_0+K_0)}} \tag{6}$$

where

$$K_J = \frac{E_J}{3(1-2v_J)} \tag{7}$$

$$G_J = \frac{E_J}{2(1+2v_J)} \tag{8}$$

It should be noted that the presence of micropores likely affects the nanoindentation results. Thus, the porosity (φ) must be introduced during homogenization:

$$K_0 = \frac{4(1-\varphi)K_cG_c}{4G_c + 3\varphi K_c} \tag{9}$$

$$G_0 = \frac{4(1-\varphi)G_c}{1 + 6\varphi\frac{K_c+2G_c}{9K_c+8G_c}} \tag{10}$$

where K_J and G_J denote the bulk and shear modulus of phase J, respectively. K_c and G_c are the bulk and shear modulus of solid particles in the clay, respectively. The bulk modulus and shear modulus can be calculated using Young's modulus E_J and Poisson's ratio v_J. K_0 and G_0 denote the bulk modulus and shear modulus of the porous matrix, respectively. The value of porosity was determined as 4.3%.

The homogenized Young's modulus E_M can be calculated as follows:
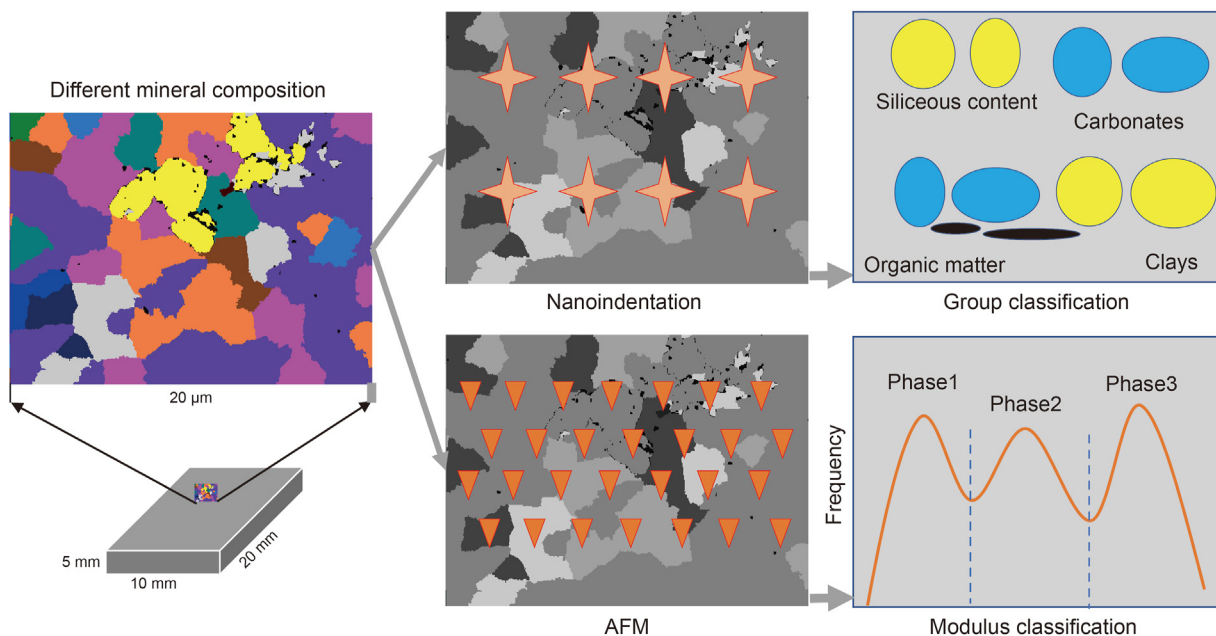
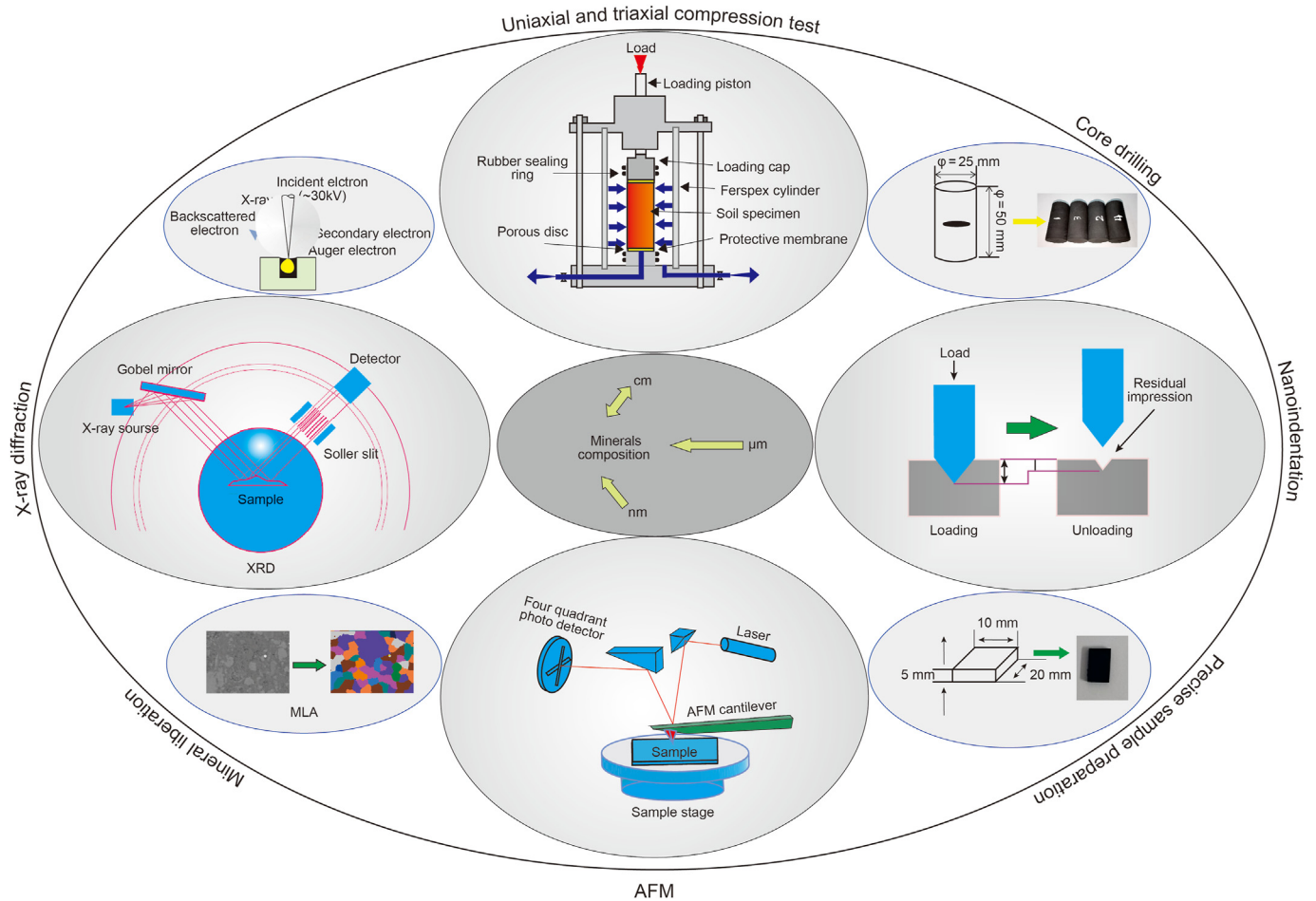**Fig. 8.** Basic upscaling methods for nanoindentation and AFM results.

Fig. 9. Experimental investigation of mechanical properties of shale at different scales.

$$E_M = \frac{9K_M G_M}{3K_M + G_M} \tag{11}$$

where K_M and G_M denote the bulk modulus and shear modulus after homogenization, respectively.

The modulus determined via the AFM was validated using different models, and the modulus for the studied samples was divided into three phases (Fig. 8). The average values of each phase were used as the E_J values during the upscaling calculation. Subsequently, the upscaled modulus could be determined using the process as that used for the nanoindentation testing.

4.1.2. Comparison of AFM and nanoindentation upscaling results

The upscaled results and uniaxial compression results were not considerably different, although the values obtained using the nanoindentation and AFM testing were slightly higher than the uniaxial testing values (Table 6). The results of nanoindentation were higher than those of the AFM, likely because the scale of AFM measurement is smaller than that for the nanoindentation. The AFM results thus contain more information, such as that pertaining to the organic matter, micropores, and nanopores, even though these components occupy only a limited area fraction in the MLA images. When the equivalent modulus of shale is calculated using the mineral composition and nanoindentation test data, the influence of the specific mineral composition and pore/fracture on the mechanical properties of shale may be neglected. Furthermore, the

mechanical parameters of all the minerals in the scanning area can be obtained using the AFM, which makes the test results more similar to the actual conditions. Compared with the AFM testing, nanoindentation leads to a higher damage to the sample surfaces, with brittle fracture occurring during the loading and unloading processes. The compression of the surfaces and generation of fractures/cracks may lead to some errors in the calculated values of the modulus and hardness.

Both the nanoindentation and AFM upscaling results exhibited a good linear relationship with the uniaxial results (Fig. 6d). Nevertheless, the AFM results exhibited a better linear relationship, with a variance of 0.9086. Even though the nanoindentation results exhibited a wide variation range, a satisfactory linear relationship can be observed if sample 2_v is excluded. Thus, the AFM and nanoindentation testing can be used to determine the mechanical properties of shale at the core scales.

4.2. Investigation of multi-scale rock mechanics

Rocks indicate different mechanical responses at different scales, according to the composition of the complex minerals, clays, and fractures (Dong and Chen, 2017). The upscaling from the nano and micrometer scale to the centimeter scale of shale can be conducted based on the multi-scale composition recognition, micro/nanomechanical testing and influence factor analysis, and multi-scale homogenization (Fig. 9). The process can gradually replace the costly and time-consuming uni/triaxial strength experiments to

determine the elastic characteristics of rocks at a micro scale. As shown in Fig. 8, the commonly used micro scale mechanical test methods include nanoindentation and AFM, which require centimeter or millimeter scale slices. The mineral composition can be determined using the MLA or XRD methods, which can help detect the content of minerals with different strengths. SEM testing can support more accurate determination of the mineral and pore structures distributions. To examine specific aspects, the correlations among the micro and macro scale mechanical parameters can be established based on the Mori–Tanaka methods. Moreover, the routine compression test can be performed to evaluate the accuracy of the upscaling results.

The advantage of the determination of the macro scale modulus via micro scale measurement is that the sample requirements are not strict. Even the debris acquired during well drilling can be used to determine the micro modulus and mineral compositions. Thus, it is easy to determine the underground mechanical properties during well drilling, and any necessary adjustment to the well orientation can be realized promptly. Furthermore, a larger number of samples can be tested owing to the non-stringent requirement pertaining to the sample sizes, thereby providing more detailed strata information.

In this work, to examine the multi-scale mechanical models of shale, the coupling of the shale components and mechanics was systematically considered. However, the actual contact types of the clay and minerals at the micro scale were not considered, and this aspect must be further examined in terms of the interface cementation mechanics. Moreover, during the upscaling process, the influence of the fluid that may saturated in the shale was not considered, which must be examined in further research. In addition, numerical methods such as discrete elements can be introduced to analyze the multi-scale coupling mechanism of the micro discrete distribution and the macro continuous distribution.

5. Conclusions

This paper proposes an integrated approach to determine the macro modulus of shale via micro mechanical testing. The upscaled Young's modulus results obtained via nanoindentation and AFM measurement exhibited a linear relationship with the uniaxial results, although the fitting of the AFM results was better.

The mineral compositions act as the medium to upscale the mechanical parameters from nano and micrometer scales to millimeter and centimeter scales. The mineral composition can be determined using the MLA and XRD techniques. The minerals must be classified into different phases to enable rapid calculations, based on the modulus similarity.

The nanoindentation testing clarifies the distribution of the Young's modulus and hardness, and the variation can be illustrated via the indentation curves. The Young's modulus obtained using the AFM has a wide variation range owing to the different compositions of the rocks, as the AFM probe is of the nanometer scale. In general, a trimodal modulus distribution for shale was identified using the AFM.

The proposed approach can be used to promptly predict the mechanical properties, such as the modulus and hardness, by using the upscaled relation between the AFM/nanoindentation results and compression test results. During well drilling, the MLA, AFM, and nanoindentation tests can be conducted to obtain the macro mechanical parameters by using the rock debris.

Acknowledgment

References

Bennett, K.C., Berla, L.A., Nix, W.D., Borja, R.I., 2015. Instrumented nanoindentation and 3D mechanistic modeling of a shale at multiple scales. Acta Geotechnica 10 (1), 1–14. https://doi.org/10.1007/s11440-014-0363-7.
Cai, J.C., Lin, D.L., Singh, H., Wei, W., Zhou, S.W., 2018. Shale gas transport model in 3D fractal porous media with variable pore sizes. Mar. Petrol. Geol. 98, 437–447. https://doi.org/10.1016/j.marpetgeo.2018.08.040.
Delafargue, A.A., 2004. Material Invariant Properties of Shales: Nanoindentation and Microporoelastic Analysis. Master thesis.
Domnich, V., Gogotsi, Y., Dub, S., 2000. Effect of phase transformations on the shape of the unloading curve in the nanoindentation of silicon. Appl. Phys. Lett. 76 (16), 2214–2216. https://doi.org/10.1063/1.126300.
Dong, G.J., Chen, P., 2017. A comparative experiment investigate of strength parameters for Longmaxi shale at the macro- and mesoscales. Int. J. Hydrogen Energy 42, 20082–20091. https://doi.org/10.1016/j.ijhydene.2017.05.240.
Fallahzadeh, S.H., Rasouli, V., Sarmadivaleh, M., 2015. An investigation of hydraulic fracturing initiation and near-wellbore propagation from perforated boreholes in tight formations. Rock Mech. Rock Eng. 48 (2), 573–584. https://doi.org/10.1007/s00603-014-0595-8.
Gathier, B., 2008. Multiscale Strength Homogenization: Application to Shale Nanoindentation. Master's dissertation. Massachusetts Institute of Technology.
Gholami, R., Elochukwu, H., Fakhari, N., Sarmadivaleh, 2018. A review on borehole instability in active shale formations: interactions, mechanisms and inhibitors. Earth Sci. Rev. 177, 2–13. https://doi.org/10.1016/j.earscirev.2017.11.002.
Gholami, R., Rasouli, V., Sarmadivaleh, M., Minaeian, V., Fakhari, N., 2016. Brittleness of gas shale reservoirs: a case study from the North Perth basin, Australia. J. Nat. Gas Sci. Eng. 33, 1244–1259. https://doi.org/10.1016/j.jngse.2016.03.013.
Gilbert, A.Q., Sovacool, B.K., Benjamin, K.S., 2014. Shale gas: better modeling for the energy mix. Nature 515, 198. https://doi.org/10.1038/515198b.
Hakala, M., Kuula, H., Hudson, J.A., 2007. Estimating the transversely isotropic elastic intact rock properties for in situ stress measurement data reduction: a case study of the Olkiluoto mica gneiss Finland. Int. J. Rock Mech. Min. 44, 14–46. https://doi.org/10.1016/j.ijrmms.2006.04.003.
Han, Q., Qu, Z., Ye, Z., 2018. Research on the mechanical behaviour of shale based on multiscale analysis. Royal Soc. Open Sci. 5 (10), 181039. https://doi.org/10.1098/rsos.181039.
Hu, C.L., Li, Z.J., 2015. A review on the mechanical properties of cement-based materials measured by nanoindentation. Construct. Build. Mater. 90, 80–90. https://doi.org/10.1016/j.conbuildmat.2015.05.008.
Huang, J.S., Griffiths, D.V., Wong, S.W., 2012. Initiation pressure, location and orientation of hydraulic fracture. Int. J. Rock Mech. Min. 49, 59–67. https://doi.org/10.1016/j.ijrmms.2011.11.014.
Ilgen, A.G., Heath, J.E., Akkutlu, I.Y., Bryndzia, L.T., Cole, D.R., Kharaka, Y.K., et al., 2017. Shales at all scales: exploring coupled processes in mudrocks. Earth Sci. Rev. 166, 132–152. https://doi.org/10.1016/j.earscirev.2016.12.013.
Josh, M., Esteban, L., Piane, C.D., Sarout, J., Dewhurst, D.N., Clennell, M.B., 2012. Laboratory characterisation of shale properties. J. Petrol. Sci. Eng. 88–89, 107–124. https://doi.org/10.1016/j.petrol.2012.01.023.
Ju, Y.W., Sun, Y., Tan, J.Q., Bu, H.L., Han, K., Li, X.S., Fang, L.Z., 2018. The composition, pore structure characterization and deformation mechanism of coal-bearing shales from tectonically altered coalfields in eastern China. Fuel 234, 626–642. https://doi.org/10.1016/j.fuel.2018.06.116.
Kivi, I.R., Ameri, M., Molladavoodi, H., 2018. An experimental investigation on deformation and failure behavior of carbonaceous Garau shale in Lurestan Basin, west Iran: application in shale gas development. J. Nat. Gas Sci. Eng. 55, 135–153. https://doi.org/10.1016/j.jngse.2018.04.028.
Lferobia, C.C., Ahmad, M., 2019. A review on the experimental techniques and applications in the geomechanical evaluation of shale gas reservoirs. J. Nat. Gas Sci. Eng. 74, 103090. https://doi.org/10.1016/j.jngse.2019.103090.
Li, C.X., Ostadhassan, M., Guo, S., Gentzis, T., Kong, L., 2018. Application of PeakForce tapping mode of atomic force microscope to characterize nanomechanical properties of organic matter of the Bakken Shale. Fuel 233, 894–910. https://doi.org/10.1016/j.fuel.2018.06.021.
Li, C.X., Ostadhassan, M., Kong, L., Bubach, B., 2019. Multi-scale assessment of mechanical properties of organic-rich shales: a coupled nanoindentation, deconvolution analysis, and homogenization method. J. Petrol. Sci. Eng. 174, 80–91. https://doi.org/10.1016/j.petrol.2018.10.106.
Li, X.D., Bhushan, B., 2002. A review of nanoindentation continuous stiffness measurement technique and its applications. Mater. Char. 48 (1), 11–36. https://doi.org/10.1016/S1044-5803(02)00192-4.
Li, Y., Wang, Z.S., Tang, S.H., Elsworth, D., 2022. Re-evaluating adsorbed and free methane content in coal and its ad- and desorption processes analysis. Chem. Eng. J. 428, 131946. https://doi.org/10.1016/j.cej.2021.131946.
Li, Y., Yang, J.H., Pan, Z.J., Tong, W.S., 2020. Nanoscale pore structure and mechanical property analysis of coal: an insight combining AFM and SEM images. Fuel 260 (15), 116352. https://doi.org/10.1016/j.fuel.2019.116352.
Li, Y., Zhang, C., Tang, D.Z., Gan, Q., Niu, X.L., Wang, K., Shen, R.Y., 2017. Coal pore size distributions controlled by the coalification process: an experimental study of coals from the Junggar, Ordos and Qinshui basins in China. Fuel 206, 352–363.

https://doi.org/10.1016/j.fuel.2017.06.028.

Liu, K., Ostadhassan, M., Bubach, B., 2016. Applications of nano-indentation methods to estimate nanoscale mechanical properties of shale reservoir rocks. J. Nat. Gas Sci. Eng. 35, 1310–1319. https://doi.org/10.1016/j.jngse.2016.09.068.

Liu, K.Q., Ostadhassan, M., Bubach, B., 2018. Application of nanoindentation to characterize creep behavior of oil shales. J. Nat. Gas Sci. Eng. 167, 729–736. https://doi.org/10.1016/j.petrol.2018.04.055.

Liu, Z.C., Zhang, F., Li, X.Y., 2019. Elastic anisotropy and its influencing factors in organic-rich marine shale of southern China. Sci. China Earth Sci. 62, 1674–7313.

Lucas, B.N., Oliver, W.C., Swindeman, J.E., 1998. The dynamics of frequency-specific, depth-sensing indentation testing. Mat. Res. Symp. Proc. 522, 3–14. https://doi.org/10.1557/PROC-522-3.

Milliken, K.L., Esch, W.L., Reed, R.M., Zhang, T., 2012. Grain assemblages and strong diagenetic overprinting in siliceous mudrocks, barnett shale (mississippian), fort worth basin, Texas. AAPG. Am. Assoc. Petrol. Geol. Bull. 96, 1553–1578.

Milliken, K.L., Olson, T., 2017. Silica diagenesis, porosity evolution, and mechanical behavior in siliceous mudstones, Mowry Shale (Cretaceous), Rocky Mountains. U.S. A. J. Sediment. Res. 87, 366–387. https://doi.org/10.2110/jsr.2017.24.

Mori, T., Tanaka, K., 1973. Average stress in matrix and average elastic energy of materials with misfitting inclusions. Acta Metall. 21, 571–574. https://doi.org/10.1016/0001-6160(73)90064-3.

Niandou, H., Shao, J.F., Henry, J.P., Fourmaintraux, D., 1997. Laboratory investigation of the mechanical behaviour of Tournemire shale. Int. J. Rock Mech. Min. 34, 3–16. https://doi.org/10.1016/S1365-1609(97)80029-9.

Oliver, W.C., Pharr, G.M., 2004. Measurement of hardness and elastic modulus by instrumented indentation: advances in understanding and refinements to methodology. J. Mater. Res. 19, 3–20. https://doi.org/10.1557/jmr.2004.19.1.3.

Pakzad, A., Simonsen, J., Yassar, R.S., 2012. Gradient of nanomechanical properties in the interphase of cellulose nanocrystal composites. Compos. Sci. Technol. 72, 314–319. https://doi.org/10.1016/j.compscitech.2011.11.020.

Pittenger, B., Erina, N., Su, C., 2014. Mechanical property mapping at the nanoscale using peakforce qnm scanning probe technique. In: Nanomechanical Analysis of High Performance Materials. Springer, pp. 31–51. https://doi.org/10.1007/978-94-007-6919-9_2.

Prasad, M., Hofmann, R., Batzle, M., Kopycinska, M.M., Rabe, U., Arnold, W., 2005. Values of Mineral Modulus of Clay. SEG Technical Program Expanded Abstracts.

Raoof, G., Henry, E., Nikoo, F., Mohammad, S., 2018. A review on borehole instability in active shale formations: interactions, mechanisms and inhibitors. Earth Sci. Rev. 177, 2–13. https://doi.org/10.1016/j.earscirev.2017.11.002.

Raoof, G., Vamegh, R., Mohammad, S., Vida, M., Nikoo, F., 2016. Brittleness of gas shale reservoirs: a case study from the North Perth basin, Australia. J. Nat. Gas Sci. Eng. 33, 1244–1259. https://doi.org/10.1016/j.jngse.2016.03.013.

Sangwal, K., 2000. On the reverse indentation size effect and microhardness measurement of solids. Mater. Chem. Phys. 63, 145–152. https://doi.org/10.1016/S0254-0584(99)00216-3.

Shea, W.T., Kronenberg, A.K., 1993. Strength and anisotropy of foliated rocks with varied mica contents. J. Struct. Geol. 15 (9–10), 1097–1121. https://doi.org/10.1016/0191-8141(93)90158-7.

Shen, W.Q., Kondo, D., Dormieux, L., Shao, J.F., 2013. A closed-form three scale model for ductile rocks with a plastically compressible porous matrix. Mech. Mater. 59 (6), 73–86. https://doi.org/10.1016/j.mechmat.2012.12.008.

Shen, W.Q., Shao, J.F., 2016. An incremental micro-macro model for porous geomaterials with double porosity and inclusion. Int. J. Plast. 83, 37–54. https://doi.org/10.1016/j.ijplas.2016.04.002.

Shukla, P., Kumar, V., Curtis, M., Sondergeld, C.H., Rai, C.S., 2013. Nanoindentation studies on shales. In: San Francisco: 47th US Rock Mechanics/Geomechanics Symposium.

Thomas, L., Lyderic, B., Benoit, C., 2016. Activated desorption at heterogeneous interfaces and long-time kinetics of hydrocarbon recovery from nanoporous media. Nat. Commun. 7, 11890. https://doi.org/10.1038/ncomms11890.

Ulm, F.J., Abousleiman, Y., 2006. The nanogranular nature of shale. Acta Geotechnica 1 (2), 77–88. https://doi.org/10.1007/s11440-006-0009-5.

Ulm, F.J., Constantinides, G., Delafargue, A., Abousleiman, Y., Ewy, R., Duranti, L., McCarty, D., 2005. Material invariant poromechanics properties of shales. In: Abousleiman, Y., Cheng, A., Ulm, F.J. (Eds.), Poromechanics III. Bio Centennial (1905-2005). A.A. Balkema Publishers, London, pp. 637–644.

Veytskin, Y.B., Tammina, V.K., Bobko, C.P., Hartley, P.G., Clennell, M.B., Dewhurst, D.N., Dagastine, R.R., 2017. Micromechanical characterization of shales through nanoindentation and energy dispersive x-ray spectrometry. Geomech Energy Environ 9, 21–35. https://doi.org/10.1016/j.gete.2016.10.004.

Wang, G.C., Ju, Y.W., Yan, Z.F., Li, Q.G., 2015. Pore structure characteristics of coal-bearing shale using fluid invasion methods: a case study in the Huainan-Huaibei Coalfield in China. Mar. Petrol. Geol. 62, 1–13. https://doi.org/10.1016/j.marpetgeo.2015.01.001.

Wawersik, W.R., Fairhurst, C., 1970. A study of brittle rock fracture in laboratory compression experiments. Int. J. Rock. Mech. Min. 7, 561–575. https://doi.org/10.1016/0148-9062(70)90007-0.

Wilkinson, S., Fenton, C., 2015. The influence of geological history on preferred particle orientation and the observed anisotropy of over consolidated UK mudrocks. In: Lollino, G., et al. (Eds.), Engineering Geology for Society and Territory, vol. 6. Springer, Cham.

Wu, T.H., Zhao, J.L., Zhang, W., Zhang, D.X., 2020. Nanopore structure and nanomechanical properties of organic-rich terrestrial shale: an insight into technical issues for hydrocarbon production. Nanomater. Energy 69, 104426. https://doi.org/10.1016/j.nanoen.2019.104426.

Xia, Y., Bigerelle, M., Marteau, J., Mazeran, E., Iost, A., 2014. Effect of surface roughness in the determination of the mechanical properties of material using nanoindentation test. Scanning 36, 134–149. https://doi.org/10.1002/sca.21111.

Xu, H., Zhou, W., Hu, Q., Yi, T., Ke, J., Zhao, A., 2021. Quartz types and silica sources and their implications for porosity evolution and rock mechanics in the Paleozoic Longmaxi Formation shale, Sichuan Basin. Mar. Petrol. Geol. 128 (9), 105036. https://doi.org/10.1016/j.marpetgeo.2021.105036.

Yang, S.Q., Jiang, Y.Z., Xu, W.Y., Chen, X.Q., 2008. Experimental investigation on strength and failure behavior of pre-cracked marble under conventional triaxial compression. Int. J. Solid Struct. 45, 4796–4819. https://doi.org/10.1016/j.ijsolstr.2008.04.023.

Zhao, S.H., Li, Y., Wang, Y.B., Ma, Z.T., Huang, X.Q., 2019. Quantitative study on coal and shale pore structure and surface roughness based on atomic force microscopy and image processing. Fuel 244, 78–90. https://doi.org/10.1016/j.fuel.2019.02.001.

Zaoui, A., 2002. Continuum micromechanics: survey. J. Eng. Mech. ASCE 128, 808–816. https://doi.org/10.1007/978-3-7091-2662-2.

Zeng, K.Y., Shen, L., 2002. A new analysis of nanoindentation load-displacement curves. Philos. Mag. A 82, 2223–2229. https://doi.org/10.1080/01418610210134422.